Geochemical Perspectives Letters

The journey of K-MORBs, told through geological, geochemical and geophysical data

L. Grenet, C. Hamelin, D. Brunelli, M. Maia, A. Briais, L. Verhoest, Z. Yu, S.C. Singh

Supplementary Information

The Supplementary Information includes:

- 1. Whole Rock: Major and Trace Elements
- 2. Minerals: Major and Trace Element Analysis and Imaging
- 3. Pyroxenes Thermobarometry and Hygrometer Calculations
- 4. Description of Samples
- Figures S-1 to S-18
- Table S-1
- Tables S-2 to S-20 (.xlsx)
- Supplementary Information References

1. Whole Rock: Major and Trace Elements

Major and trace elements of the groundmass were measured at the PSO/IUEM (Pôle Spectrométrie Océan, Institut Universitaire Européen de la Mer, Brest, France). For major element analysis, samples were crushed and sieved, the size fraction of 2-1 mm was retained. Phenocrysts and fractions with alteration were manually removed. A mass of 250 mg of the 2-1 mm fraction was dissolved in closed screw-top Teflon vessels (Savillex), at about 90 °C for 24h using 1 ml of HNO_3 and 3 ml of HF. Then 96 ml of H_3BO_3 were added to neutralise the effect of HF (Cotten *et al.*, 1995). Major element compositions were measured by an inductively coupled plasma-atomic emission spectrometer (ICP-AES) using Horiba Jobin Yvon® Ultima 2. Calibrations were made using international standards JB2, ACE, ME, and WSE, and internal standards CB2, BELC, CB15 and CB18.

Trace elements were analysed with a high-resolution inductively coupled plasma mass spectrometer (HR-ICPMS) ELEMENT XR, ThermoFisher Scientific. Samples were prepared following Barrat *et al.* (1996) protocol. Powdered samples (100 mg) were dissolved in screw-top Teflon vessels (Savillex) using an HF-HNO_3 mixture and evaporated to dryness. Dry residues were then dissolved in 40 g of 6N HCl. An aliquot of 1 ml of this solution was collected; a solution of pure Tm was added and then evaporated to dryness. Samples were taken up in 2.5 % HNO_3 for analysis on the ICP-MS. Calibrations were made using BCR2 and WSE standards.

2. Minerals: Major and Trace Element Analysis and Imaging

Major element compositions were determined by electron probe microanalysis (EPMA), using a Cameca SX100 electron microprobe (Microsonde Ouest, Brest, France). Analyses were performed on carbon-coated polished thin sections under the following conditions: 15 kV accelerating voltage, 20 nA beam current, spot size of 1 µm and 10 s (20 s for F and 30 s for Ti) counting time on the peak. Standards were natural albite (Na), forsterite (Mg), apatite (F, P), wollastonite (Si, Ca), corundum (Al), orthoclase (K), $MnTiO_3$ (Ti, Mn), andradite (Fe), pyromorphite (Cl), Cr_2O_3 (Cr), and NiO (Ni). Electron microprobe transects were performed on clinopyroxene phenocrysts, each spot separated by 10 µm (for small crystals and transversal profiles) to 20 µm (for longitudinal profiles). The error in an analysis is considered to be 1 % of the value. For mapping, we used 1 to 2 µm pixel size and 100 s dwell time per pixel, measuring nine to ten elements per map. The size of maps varies from 253 x 253 µm to 1428 x 2023 µm.

The target minerals for trace element analysis were chosen by combining microscope observations and scanning electron microscope (SEM). Thick section imaging was carried out using JEOL JSM-6010LA InTouchScope SEM at 20 kV in the Dipartimento di Scienze Chimiche e Geologiche of Modena (Italy).

The trace elements were measured on clinopyroxene phenocrysts. They were measured by laser ablation inductively coupled mass spectrometer (LA-ICP-MS) at Centro Interdipartimentale Grandi Strumenti (CIGS, Modena), using Thermo Scientific iCAP TQ ICP-MS. Analyses were performed on 90 µm-thick polished thin sections. Analyses were run over 30 s, using 100 % energy output, a 10 Hz repeat rate, and a 55 µm spot size. Three standards (NIST 612, NIST 614 and MLB3) were analysed at the beginning and end of each session. Data were normalised with the SiO_2 of each crystal as an internal standard obtained by averaging three analyses realised by EPMA. The number of crystal targets was limited by the size of the minerals, which must be larger than 55 µm. Areas of analysis must be flat, without fracture or inclusion to avoid diffusive effects and uniquely measure the mineral composition. When the conditions were met, we performed at least two points of analysis, one in the centre and one in the rim to investigate if the composition of the crystals varies during their crystallisation.

3. Pyroxene Thermobarometry Calculations

Thermobarometric calculations using the clinopyroxene major compositions, from thin section analysis, were performed using an iterative approach adapted from Neave and Putirka (2017). The temperature was estimated using Equation 33 from Putirka (2008), this model has a standard estimated error (SEE) of 45 °C. The pressure was estimated using Neave

and Putirka (2017) model, adapted to alkaline hydrated lavas and independent of the water content. This model has a SEE of 1.4 kbar.

Temperature and pressure of crystallisation were calculated for clinopyroxenes using in situ analyses and profiles. The equilibrium between the clinopyroxenes and the whole rock was estimated by calculating the $K_D(Fe–Mg)_{cpx–liq}$ from the whole rock with Equation 35 of Putirka (2008). We consider that, the equilibrium was reached for a $K_D = 0.03 \pm 0.08$ (Wieser *et al.*, 2023). Diopside-Hedenbergite (DiHd), Enstatite-Ferrosilite (EnFs), and Calcium-Tschermak (CaTs) component equilibria were tested using Mollo *et al.* (2013) (for DiHd and EnFs) and Putirka (1999) (for CaTs). We used thresholds of 0.06, 0.05, and 0.03 for the ΔDiHd, ΔEnFs, and ΔCaTs components, respectively, corresponding to the SEE reported by Mollo *et al.* (2013). Only the clinopyroxene-whole rock pairs, which present equilibrium for all tested parameters, were kept and considered as meaningful for P-T petrological interpretations. The clinopyroxenes are sector zoned; one zone is Si-Mg-rich, and the other is Al-Ti-rich. According to Zhou *et al.* (2021), in sector-zoned clinopyroxenes, the SiO_2-rich sectors are closer to real equilibrium than Al_2O_3-rich sectors. Hence, only analyses realised in Si-Mg-rich sectors are kept for P-T.

4. Description of Samples

Seamount

The samples collected from the seamount are sparsely plagioclase-phyric basalts with a microlithic groundmass dominated by plagioclase with olivine. They are moderately fresh, with few vesicles. Those samples are characterised by phenocrysts of plagioclases euhedral to subhedral. Some phenocrysts have sieve texture with external resorption. They frequently have elongated or small circular inclusions. Numerous microphenocrysts are present, they have an acicular or skeletal shape. Olivine phenocrysts are rare and are subhedral to skeletal. Most olivine crystals are subhedral to skeletal microphenocrysts, forming glomerophyres with plagioclases.

Cone

The samples collected from the cone (SMA1974-278 and SMA1974-279), are porphyric alkaline basalts, dominated by clinopyroxene phenocrysts with olivine phenocrysts often organised as glomerophyres (Fig. S-8). Both samples are moderately fresh and vesicular. Clinopyroxene phenocrysts are euhedral to subhedral. They are sector-zoned and have oscillatory zoning. Olivine phenocrysts are mostly skeletal, the smallest are subhedral.

The groundmass is different between both samples. The groundmass of SMA1974-278 is glassy with clinopyroxene microliths, while the groundmass of SMA1974-279 is almost entirely crystallised and composed by microliths of clinopyroxene and plagioclase (Fig.S-8 c, d). In both samples, microliths of amphibole and biotite are present around vesicles or between glomerocrysts (Fig. S-8 e, f). Amphiboles are frequently found in small patches within the matrix of SMA1974-278 and sometimes as small needles growing on the surface of larger clinopyroxenes. They have a rhombus-shape. Microliths of biotite are present as small needles.

Narrow ridge

The samples from the narrow ridge are aphyric basalts. They are moderately fresh; some cracks and vesicles are filled by iron hydroxides. Phenocrysts of plagioclase and olivine are almost absent and are sometimes present as glomerophyres. The groundmass is microlithic, composed by plagioclases, without clear foliation. Plagioclase microphenocryts are acicular or skeletal and olivines are subhedral to skeletal.

Axial volcanic ridge

The samples from the axial volcanic ridge are an aphyric basalts. The sample are moderately fresh; some cracks are filled by iron hydroxides. Microphenocrysts of plagioclase and olivine are numerous, while phenocrysts are almost absent. The groundmass is microlithic, composed by plagioclases, without clear foliation. Plagioclase microphenocrysts are acicular or skeletal and olivines are subhedral to skeletal. Glomerophyres of plagioclases and olivines are frequent.

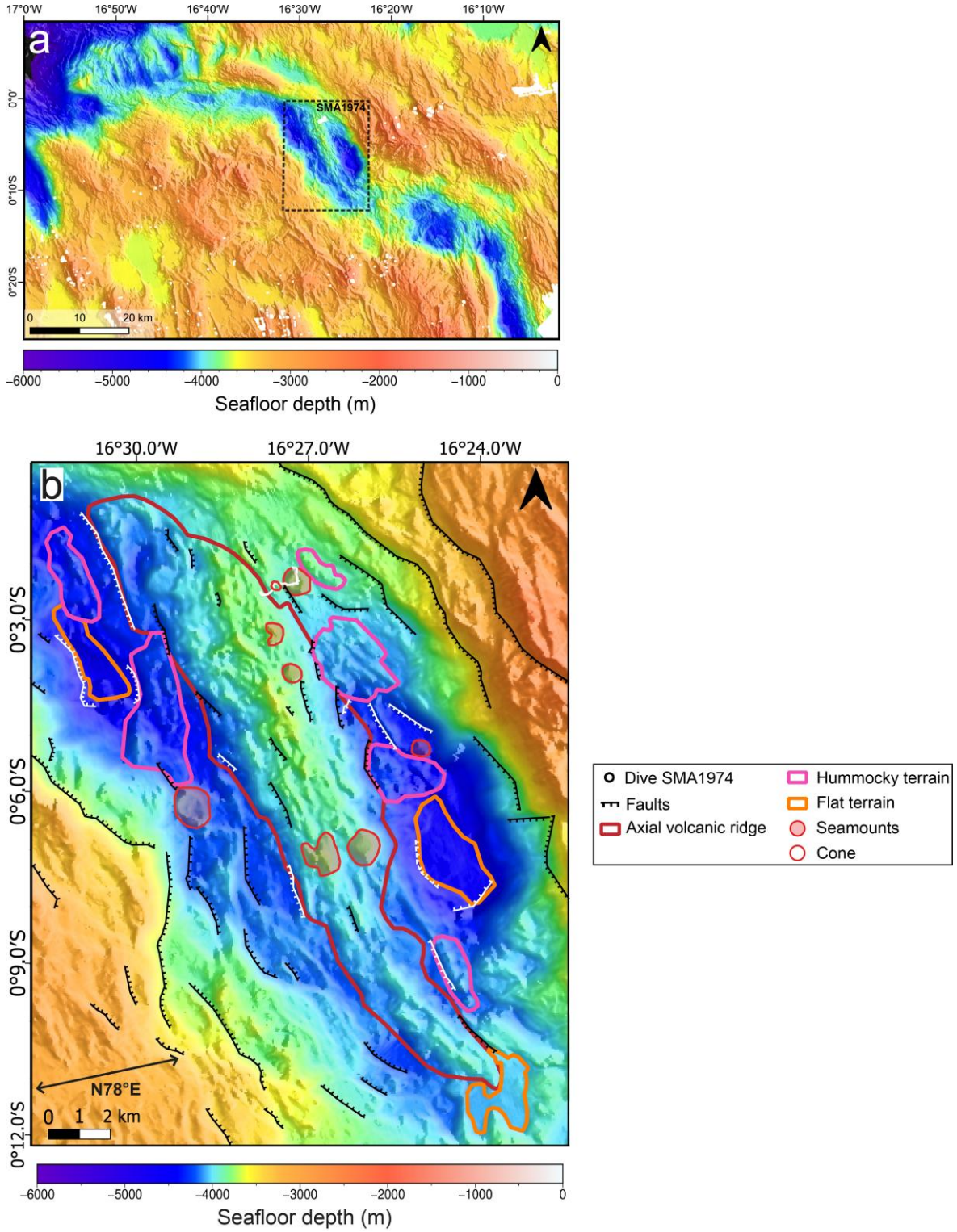

Figure S-1 Bathymetric and structural maps. **(a)** Bathymetric map, combining swath bathymetry collected during the SMARTIES cruise and previous cruises. The black dashed rectangle outlines the segment RC2. **(b)** Main volcano-tectonic features of segment RC2 reported on the bathymetric map, including the axial volcanic ridge (red line), hummocky (pink line) and flat (orange line) volcanic terrains, seamounts (brownish surfaces), the cone explored during dive SMA1974, and faults. Modified from Grenet *et al.* (2025).

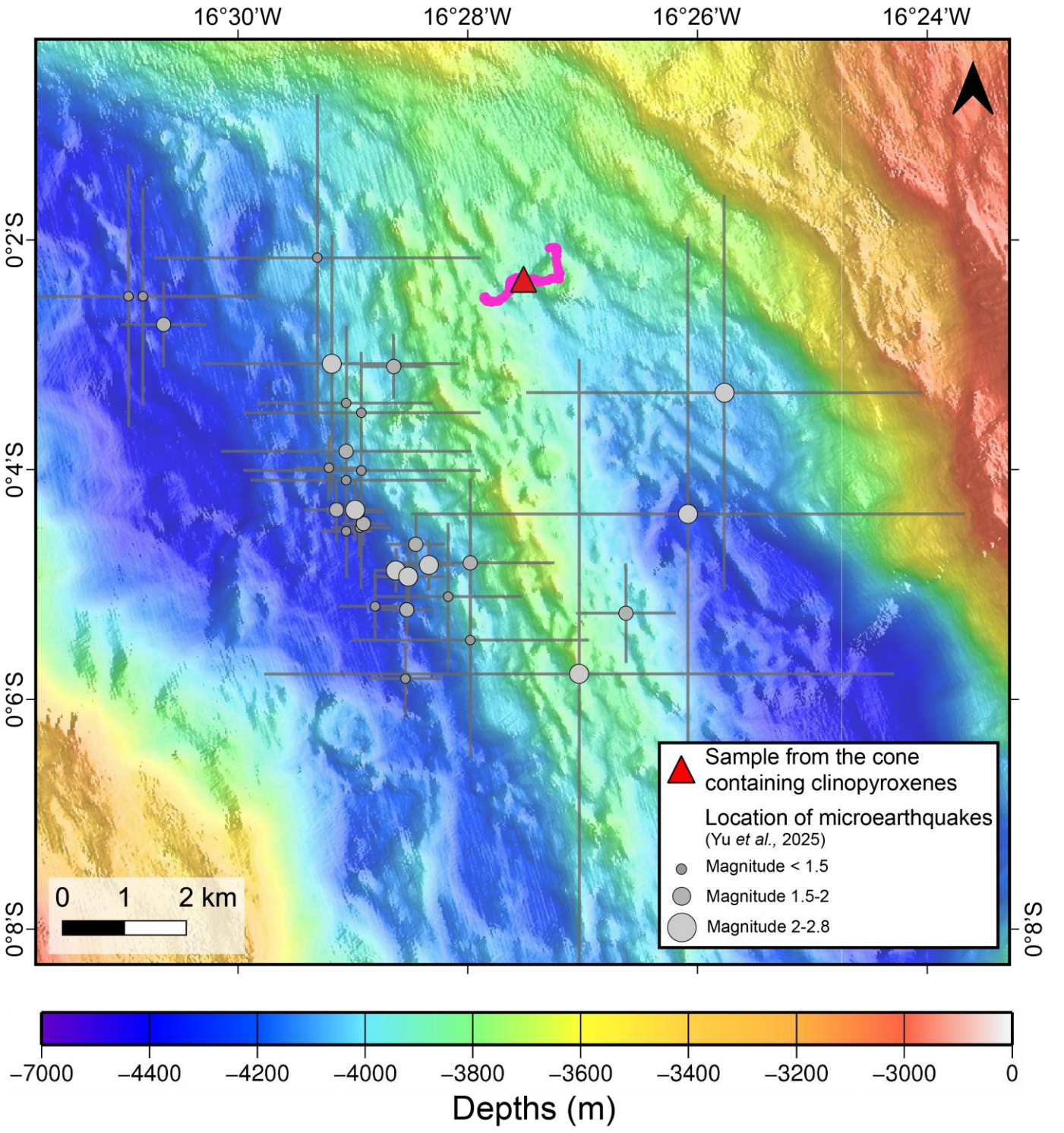

Figure S-2 Bathymetric map of the segment RC2 with the locations of the dive SMA1974 (pink track), the samples containing the studied clinopyroxenes, and the microearthquakes from Yu *et al*. (2025). The location error is represented by the lines.

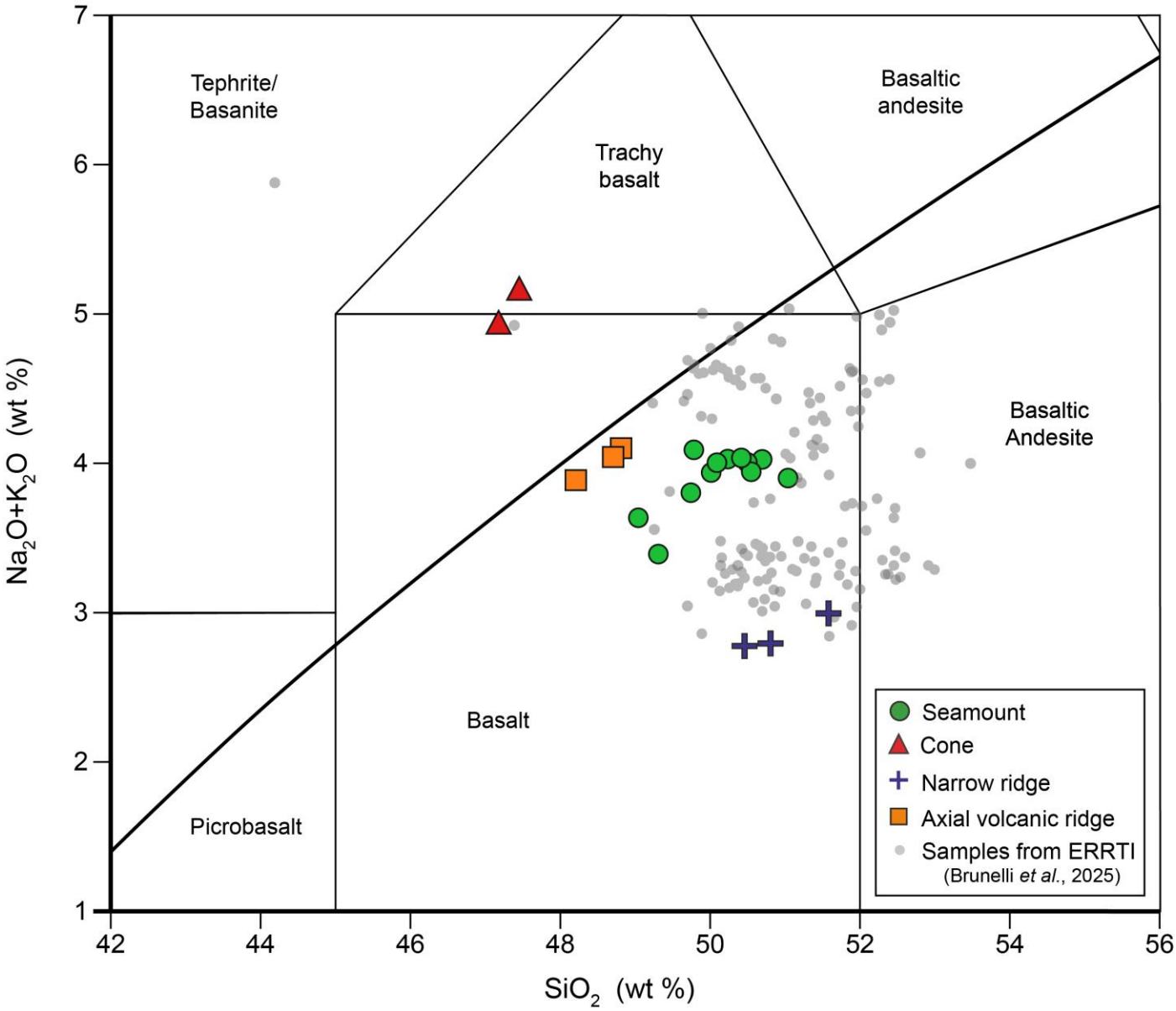

Figure S-3 Basaltic glass and whole rock compositions of the ERRTI samples collected during SMARTIES cruise. Total alkali *versus* silica (wt. %). Seamount and AVR data are from Brunelli *et al.* (2025).

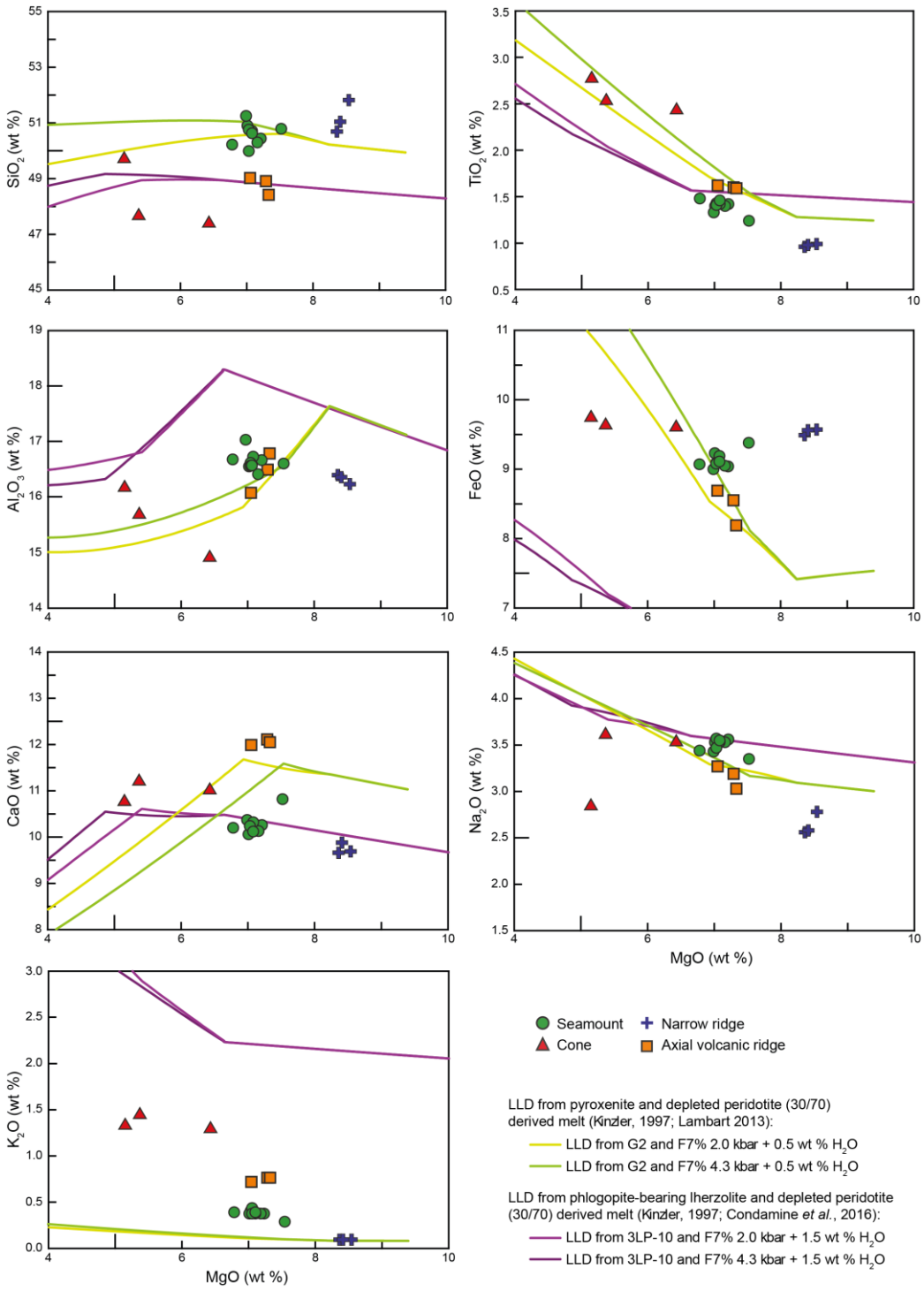

Figure S-4 Major element composition *vs.* MgO of basaltic glass and whole rock compositions of the samples collected during the dive SMA1974. Calculated LLD calculated with Petrolog3 using Danyushevsky and Plechov (2011) from mixing between a depleted peridotite and various sources: light green and green are a mixing between 70 % of aggregated melt at average melting of 7 % of a depleted peridotite (Kinzler, 1997) with 30 % melt from partial melting of eclogite G2 (Lambart, 2017); light and dark purple are a mixing between 70 % of aggregated melt at average melting of 7 % of a depleted peridotite (Kinzler, 1997) with 30 % melt from partial melting of a phlogopite-bearing lherzolite (3LP-10) (Condamine *et al.*, 2016).

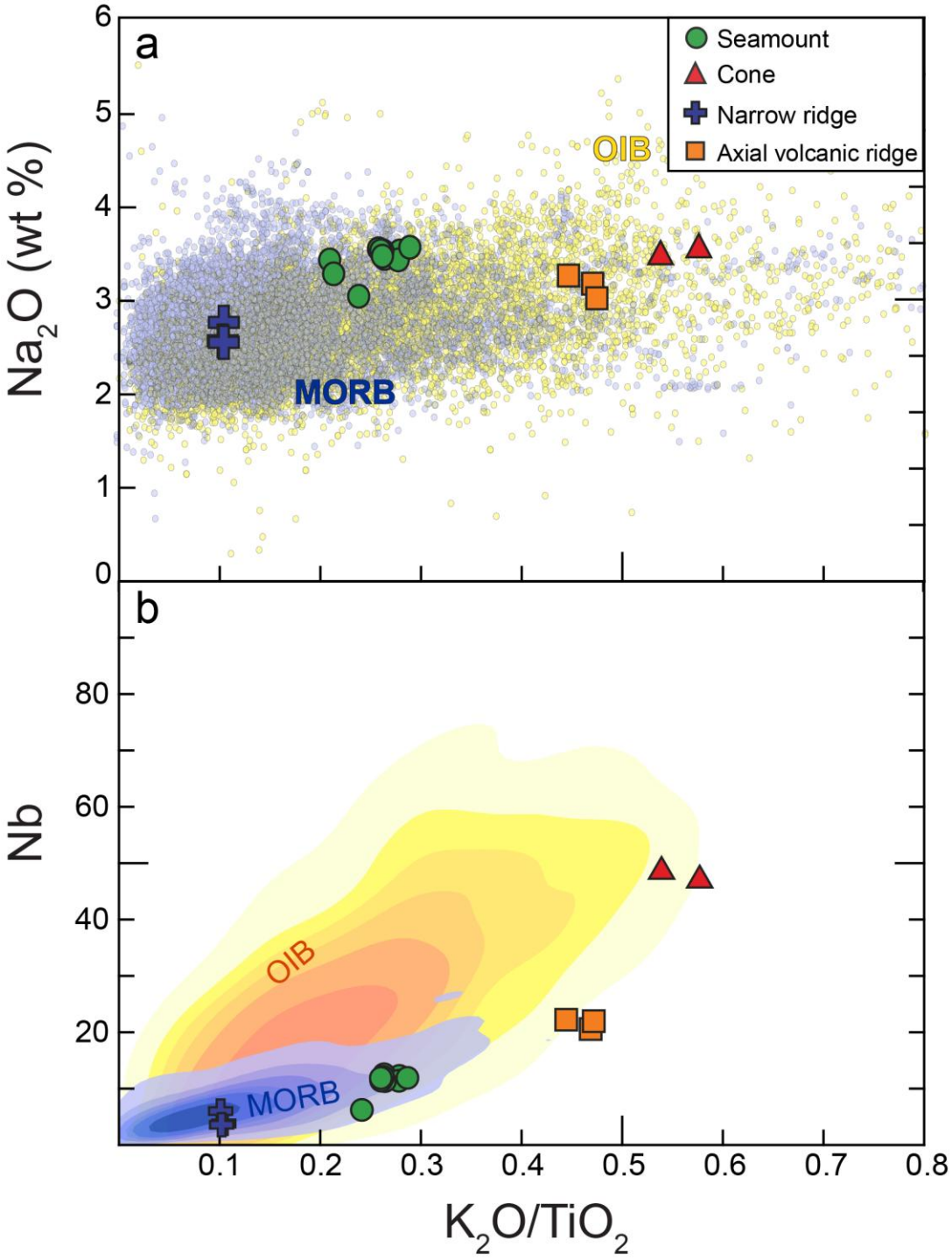

Figure S-5 Plots of Na_2O **(a)** and Nb (in ppm) **(b)** versus K_2O/TiO_2 for samples from dive SMA1974. The mid-oceanic ridge basalts (MORB) and ocean island basalts (OIB) fields represent the distribution of the composition of oceanic basalts from global data sets. In **(a)** there are 22,183 samples from PetDB for MORBs and 8,535 samples from GEOROC for OIBs. In **(b)** there are 9,289 samples for MORBs and 5,251 samples for OIBs, both from GEOROC. The different fields correspond to proportions of the sample population from the darkest colours to the lightest: 30 %; 50 %; 60 %; 70 %; 80 % and 90 %.

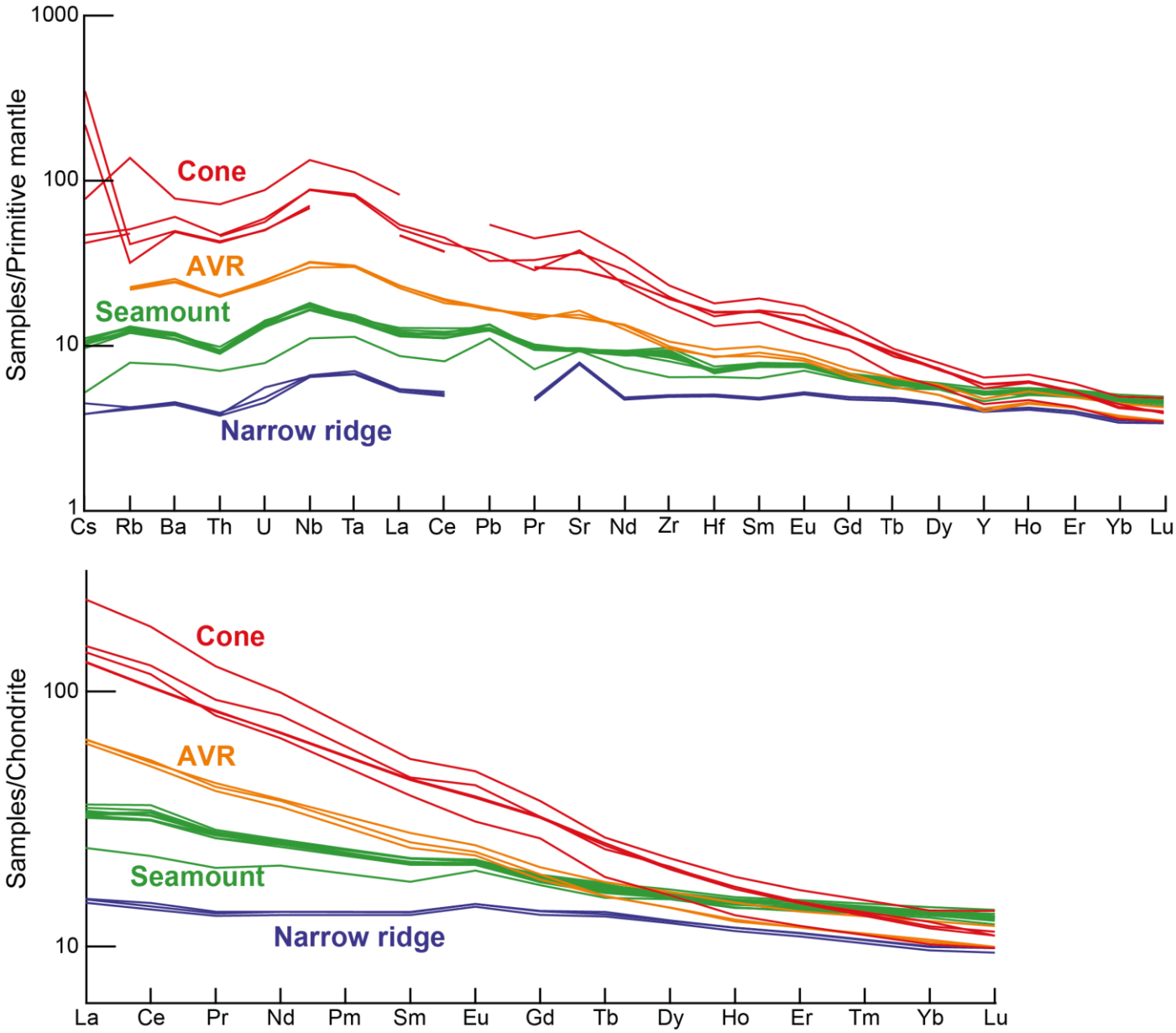

Figure S-6 Extended trace element patterns normalised to Primitive Mantle (Sun and McDonough, 1989) and REE normalised to chondrite (Sun and McDonough, 1989) of basaltic glass and whole rock trace compositions of the samples collected during the dive SMA1974. Seamount and AVR data are from Brunelli *et al*. (2025).

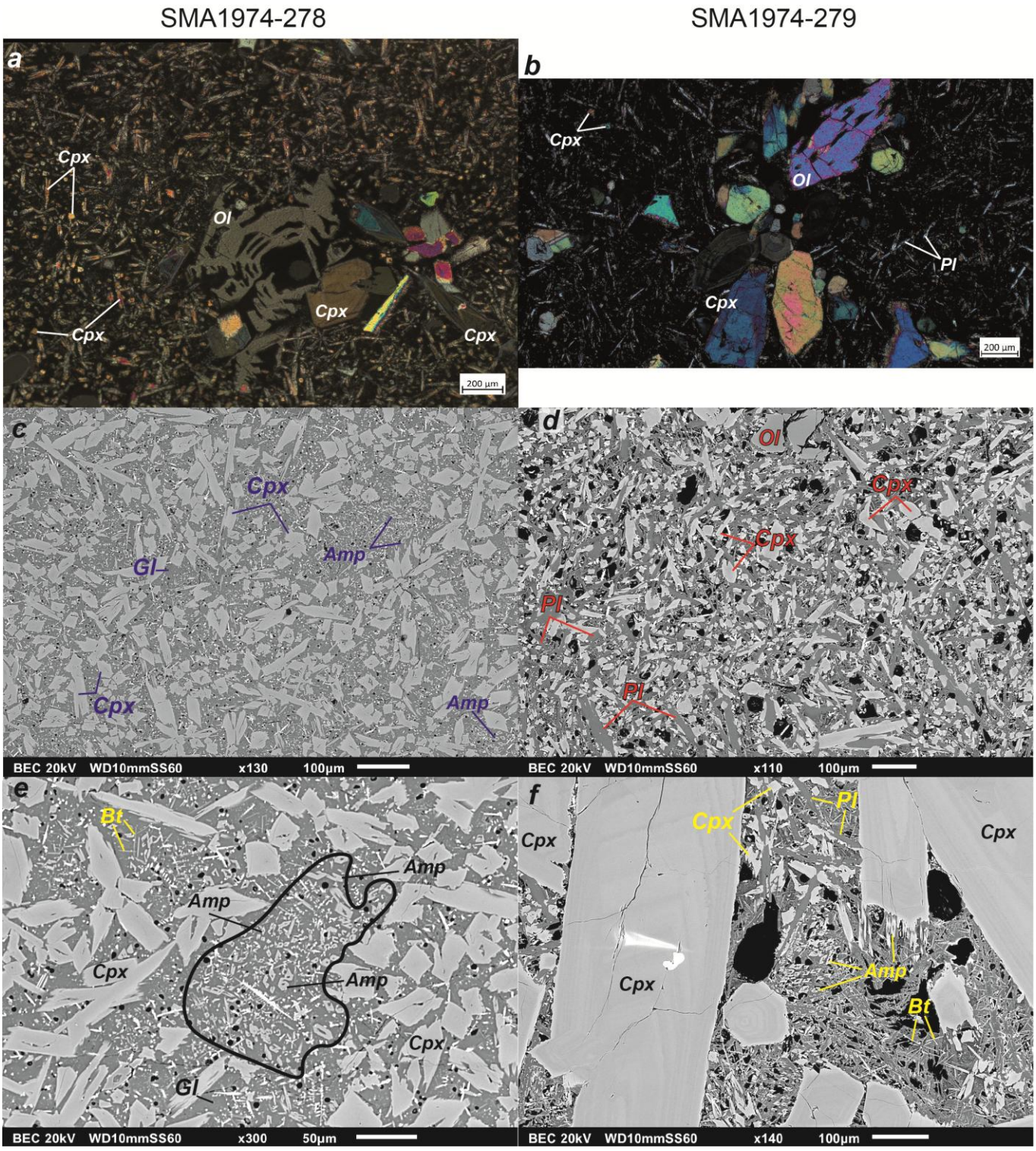

Figure S-8 Images of sample SMA1974-278 on the left of the plate (a. c. e. g) and of sample SMA1974-279 on the right (b. d. f). Microscope images in cross-polarised light (a-b) and Backscatter Scanning Electron Microscope images (c-g). **(a)** Glomerophyre composed of phenocrysts of skeletal and small olivines and zoned clinopyroxenes. The groundmass is mainly composed of microliths of clinopyroxene. **(b)** Glomerophyre composed of phenocrysts of skeletal and small olivines and zoned clinopyroxenes. The groundmass is composed of microliths of clinopyroxenes and plagioclases. **(c)** Glassy groundmass with numerous microliths of clinopyroxenes and microliths of amphiboles. **(d)**

Microcrystalline groundmass composed of microliths of clinopyroxenes and plagioclases. The black zones are vesicles. **(e)** The black line delimits a group of amphiboles characterized by their rhombus-shape. Some needles are visible in the glass, which are possibly biotites. **(f)** Numerous small biotites are presented, located between phenocrysts of clinopyroxenes; grouped amphiboles are also present, some seem to be in the extension of a clinopyroxene.

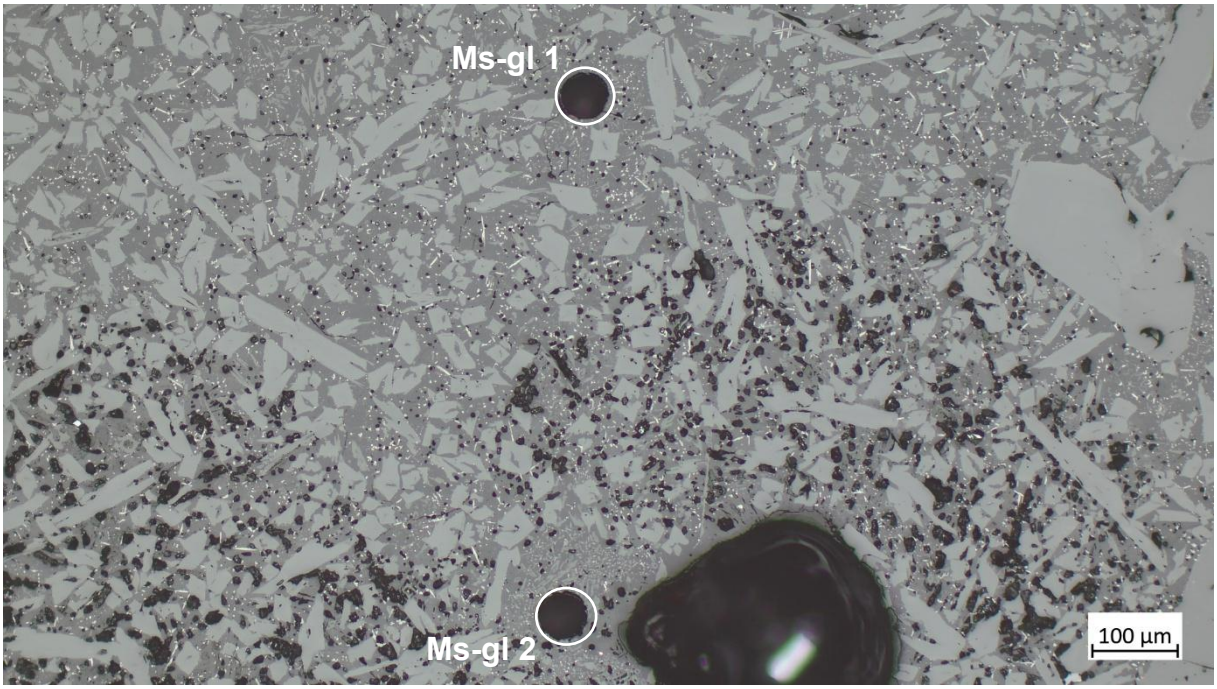

Figure S-9 Laser points of mesostasis glass (Ms-gl) 1 and 2 from sample SMA1974-278.

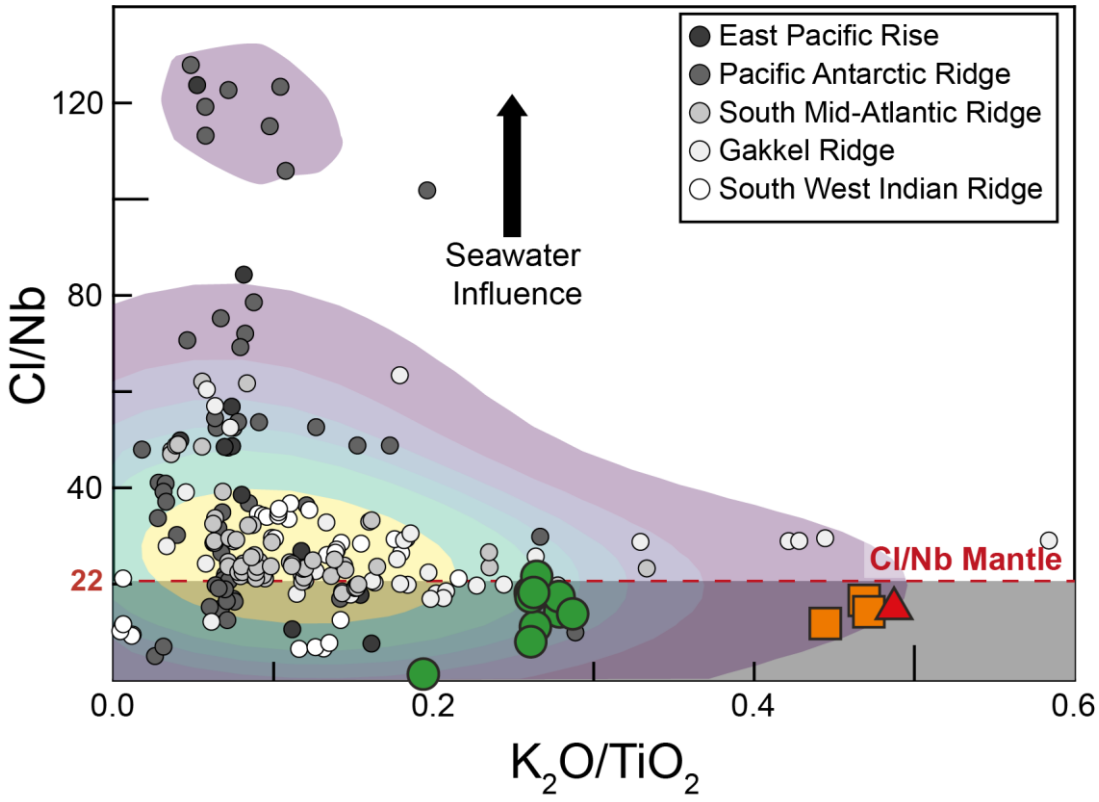

Figure S-10 Volatiles and incompatible elements versus K_2O/TiO_2 ratio for samples from dive SMA1974 and for fast to ultra-slow spreading ridges: East Pacific ridge (9-14°) (Marschall *et al.*, 2017); East Pacific ridge Siqueiros (Marschall *et al.*, 2017); southern Mid-Atlantic Ridge (Van Der Zwan *et al.*, 2017); Gakkel ridge (Van Der Zwan *et al.*, 2017) and Southwest Indian ridge (Kendrick *et al.*, 2017; Marschall *et al.*, 2017; Wang *et al.*, 2021). The Cl/Nb mantle ratio is from Van der Zwan *et al.* (2017).

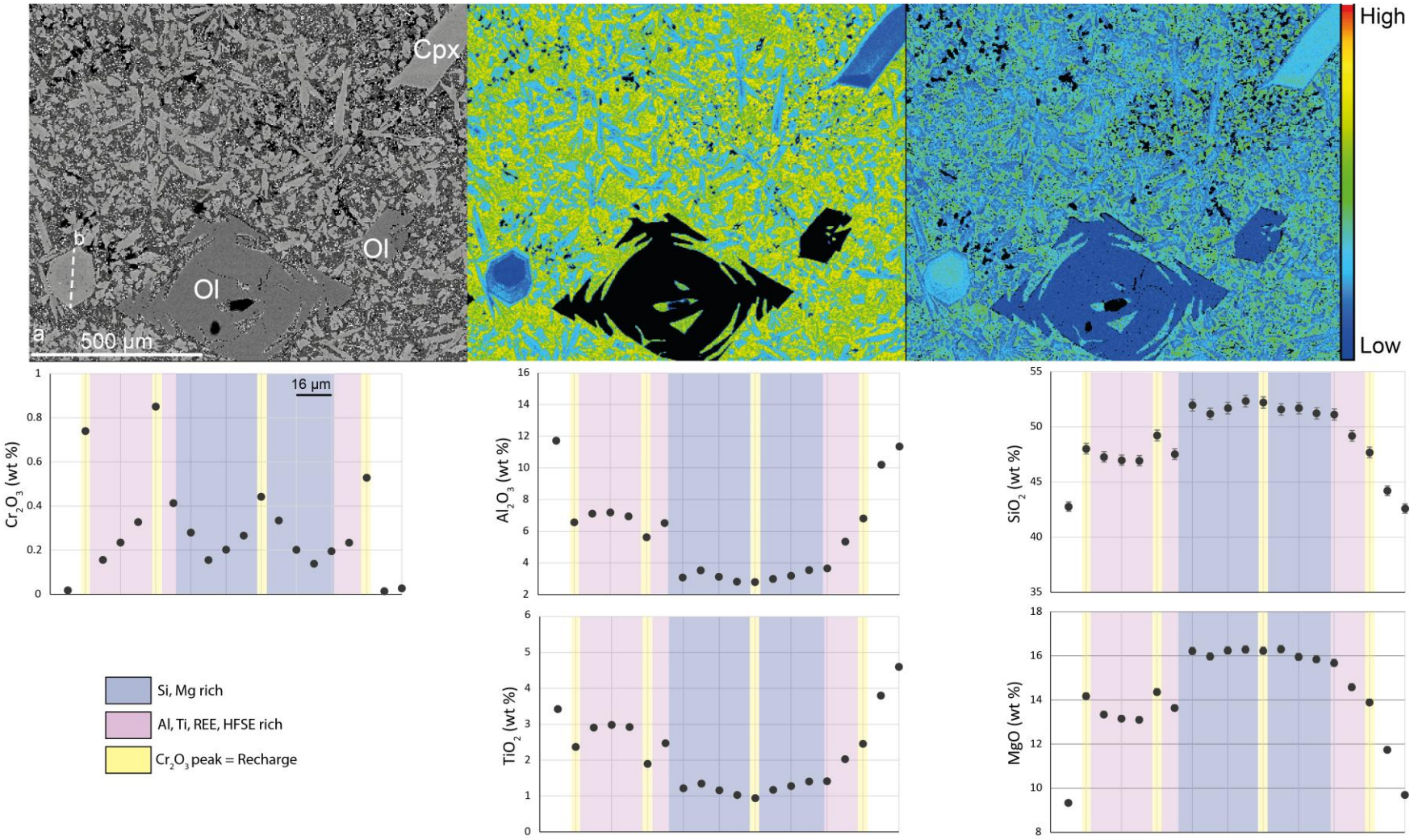

Figure S-11 Sample SMA1974-278. Backscatter electron (BSE) image and major element maps (Al and Si) of olivine and diopside phenocrysts obtained by electron microprobe. The dashed line marks the trace of the profile analysis. Electron microprobe profiles of Cr_2O_3, Al_2O_3, SiO_2, TiO_2 and MgO contents along a-b profile. Measurements at 10 µm step. The error bar represents 1 % of the value obtained; it is included in the symbol for Cr_2O_3, Al_2O_3 and TiO_2. The dark purple area represents Si-Mg-rich sector, the pink the Al-Ti-rich sector and the white zones is the outermost rim. Peaks in Cr_2O_3 are present in yellow on the profile. Cpx: clinopyroxene; Ol: olivine.

Table S-1 Non-modal batch melting aggregated melt calculated for trace element modelling.

	Starting composition	Mineral abundance	Melting mode	Partition coefficient	Mixing
D-DMM spinel	D-DMM (Workman and Hart, 2005)	0.53 Ol + 0.27 Opx + 0.17 Cpx + 0.03 Sp (Hellebrand, 2002)	-0.06 Ol + 0.28 Opx + 0.67 Cpx + 0.11 Sp (Hellebrand *et al.*, 2002)	Duvernay *et al.*, (2024)	
D-DMM garnet	D-DMM (Workmann *et al.*, 2005)	0.57 Ol + 0.21 Opx + 0.13 Cpx + 0.09 Gt (Hellebrand *et al.*, 2002)	0.04 Ol - 0.19 Opx + 1.05 Cpx + 0.11 Gt (Hellebrand *et al.*, 2002)	Duvernay *et al.*, (2024)	
E-DMM spinel	E-DMM (Workmann *et al.*, 2005)	0.53 Ol + 0.27 Opx + 0.17 Cpx + 0.03 Sp (Hellebrand *et al.*, 2002)	-0.06 Ol + 0.28 Opx + 0.67 Cpx + 0.11 Sp (Hellebrand *et al.*, 2002)	Duvernay *et al.*, (2024)	
E-DMM garnet	E-DMM (Workmann *et al.*, 2005)	0.57 Ol + 0.21 Opx + 0.13 Cpx + 0.09 Gt (Hellebrand *et al.*, 2002)	0.04 Ol - 0.19 Opx + 1.05 Cpx + 0.11 Gt (Hellebrand *et al.*, 2002)	Duvernay *et al.*, (2024)	
D-DMM + pyroxenite	Recycled oceanic crust, G2 (Lambart, 2017)	0.75 Cpx + 0.25 Grt (Pertermann *et al.*, 2004)	-0.51 Ol + 0.86 Opx + 0.57 Cpx + 0.11 Gt (Borghini *et al.*, 2017)	Pertermann *et al.*, (2004)	1 % F Sp-D-DMM; 1 % F Gt-D-DMM; 4 % F G2
D-DMM + phlogopite	Phlogopite-bearing lherzolite source, BD 2348 PP lherzolite (Grégoire *et al.*, 2002)	0.67 Ol + 0.29 Opx + 0.01 Cpx + 0.01 Sp + 0.03 Phl (Grégoire *et al.*, 2002)	-0.58 Ol + 0.56 Opx + 0.47 Cpx + 0.05 Sp + 0.49 Phl (Condamine and Médard, 2014)	Condamine *et al.*, (2022)	1 % F Sp-D-DMM and 1 % F Gt-D-DMM; 4 % F BD 2348 PP

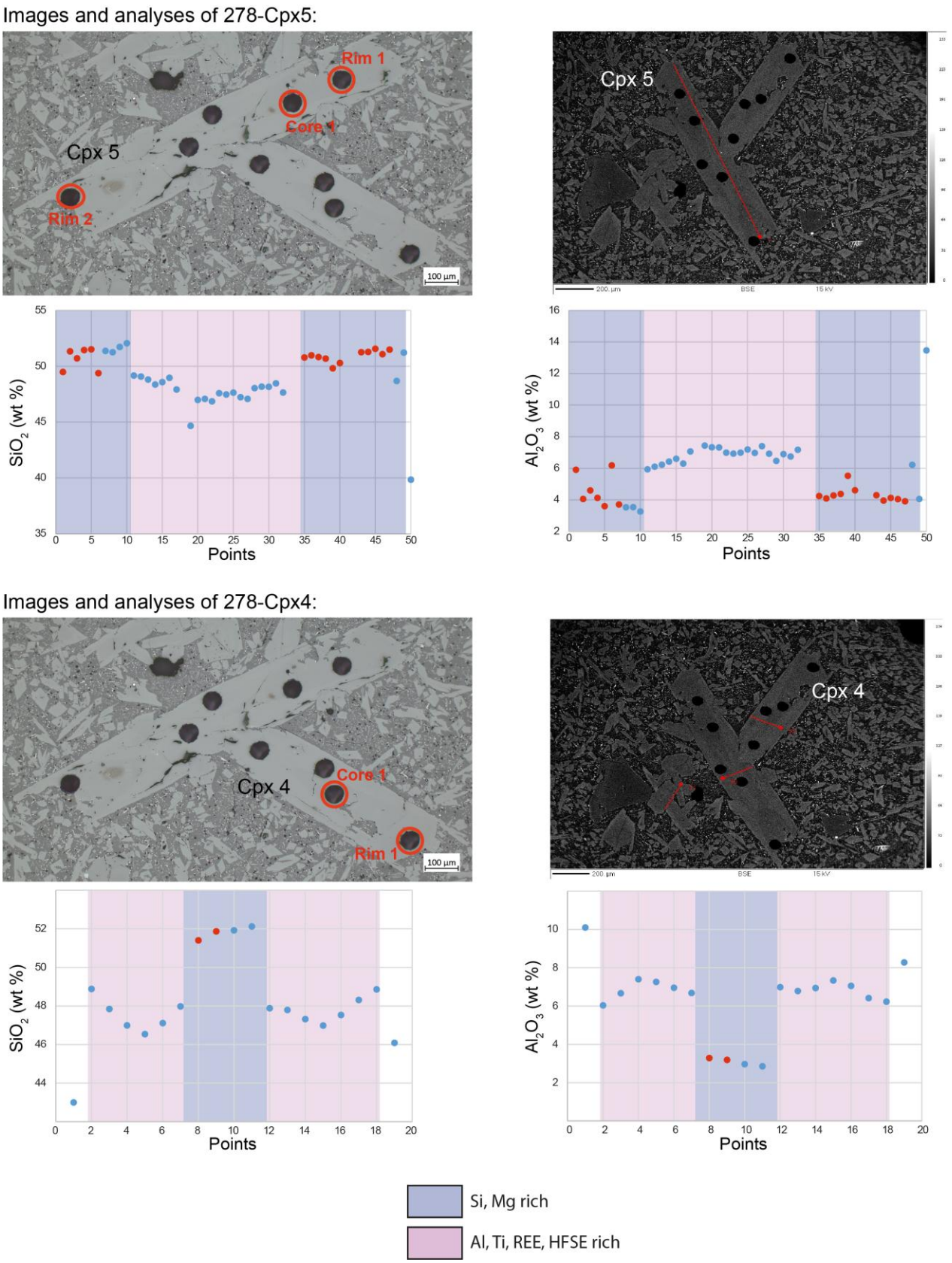

Figure S-13 BSE images and analysis profiles of Cpx5 and Cpx4 from SMA1974-278 used for geothermobarometric calculations. The red dots on the profiles are the points used for the geothermobarometric calculations (see Table S-20).

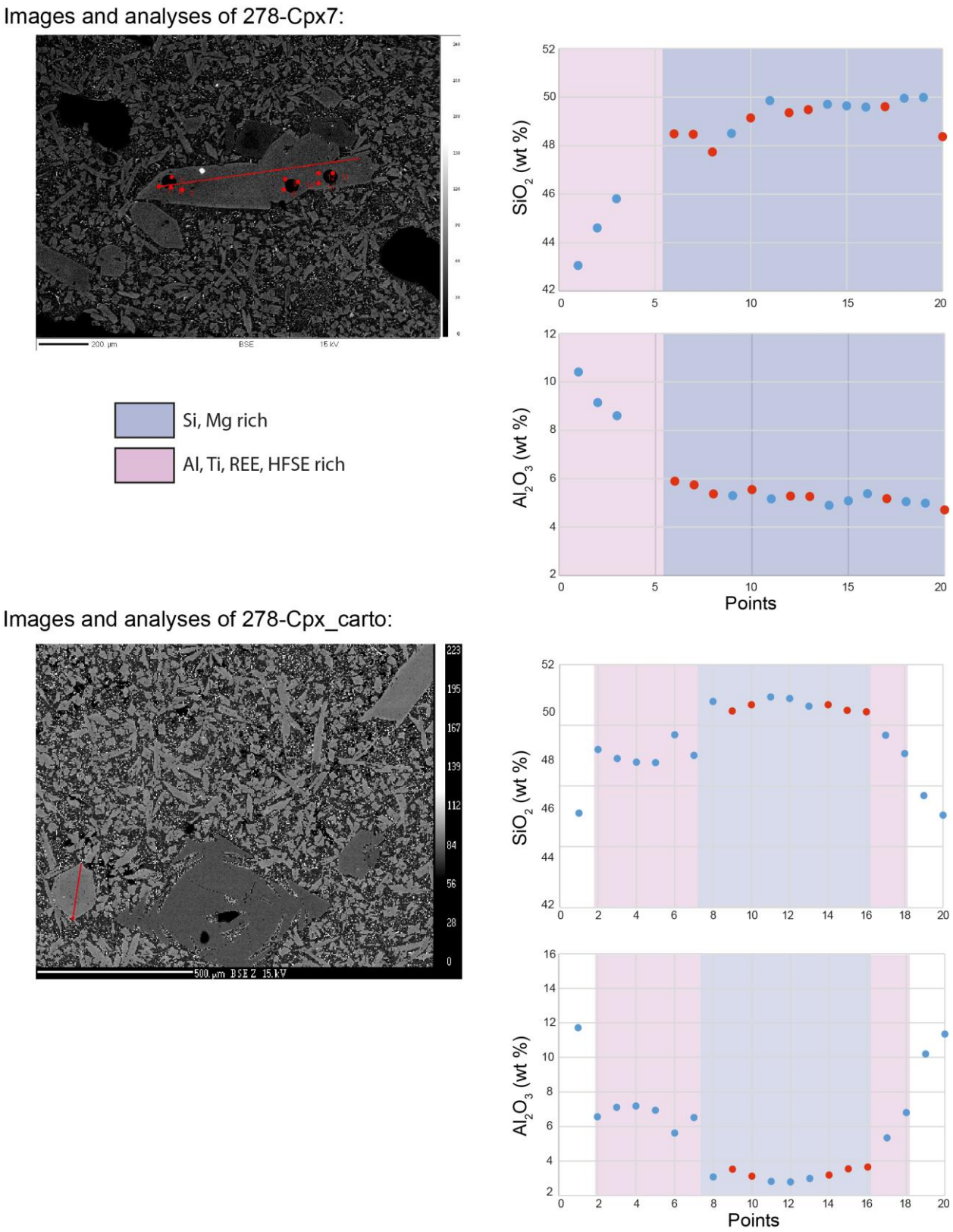

Figure S-14 BSE images and analysis profiles of Cpx7 and Cpx_carto from SMA1974-278 used for geothermobarometric calculations. The red dots on the profiles are the points used for the geothermobarometric calculations (see Table S-20).

Images and analyses of 278-Cpx_5-4:

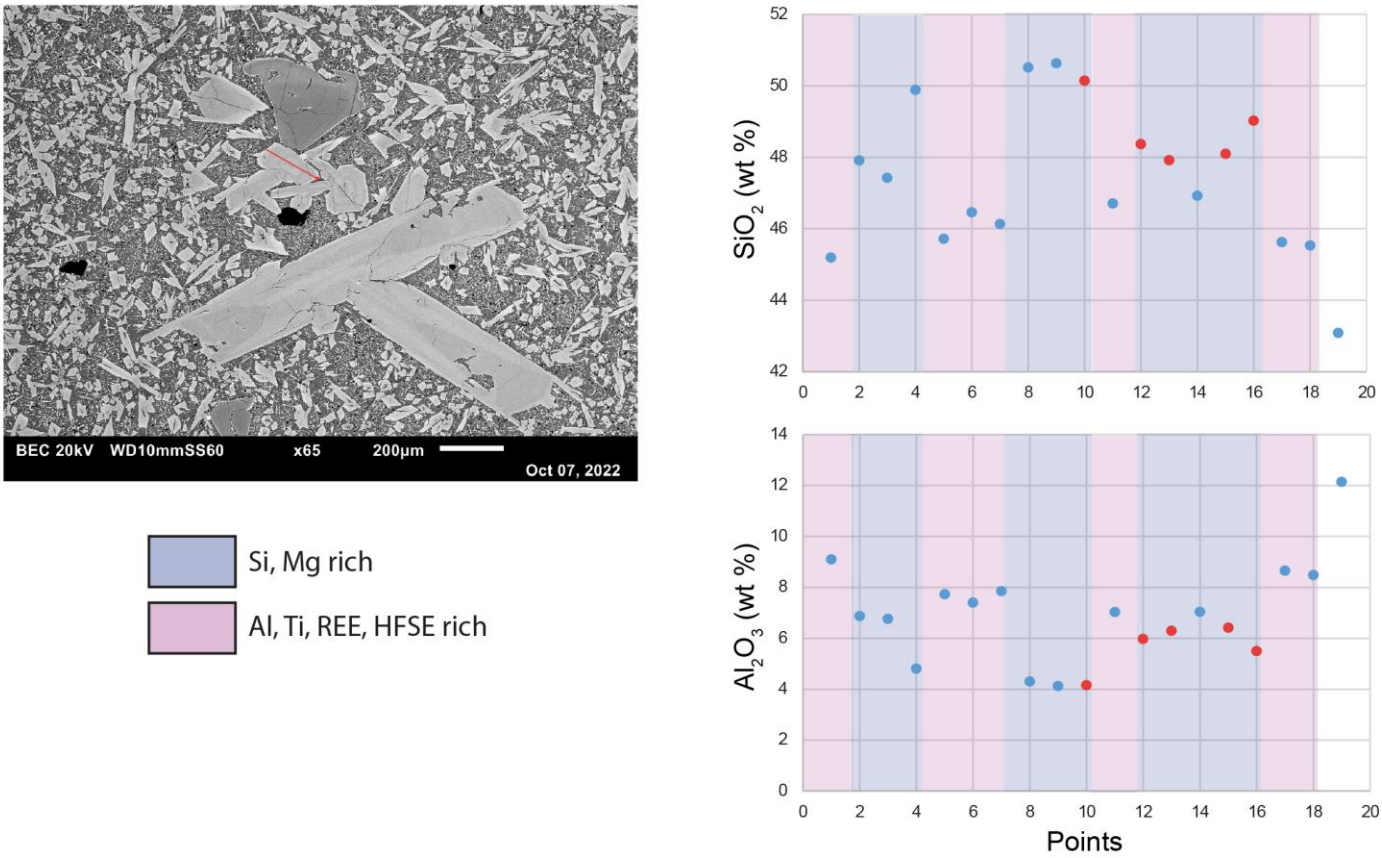

Figure S-15 BSE images and analysis profiles of Cpx5-4 from SMA1974-278 used for geothermobarometric calculations. The red dots on the profiles are the points used for the geothermobarometric calculations (see Table S-20).

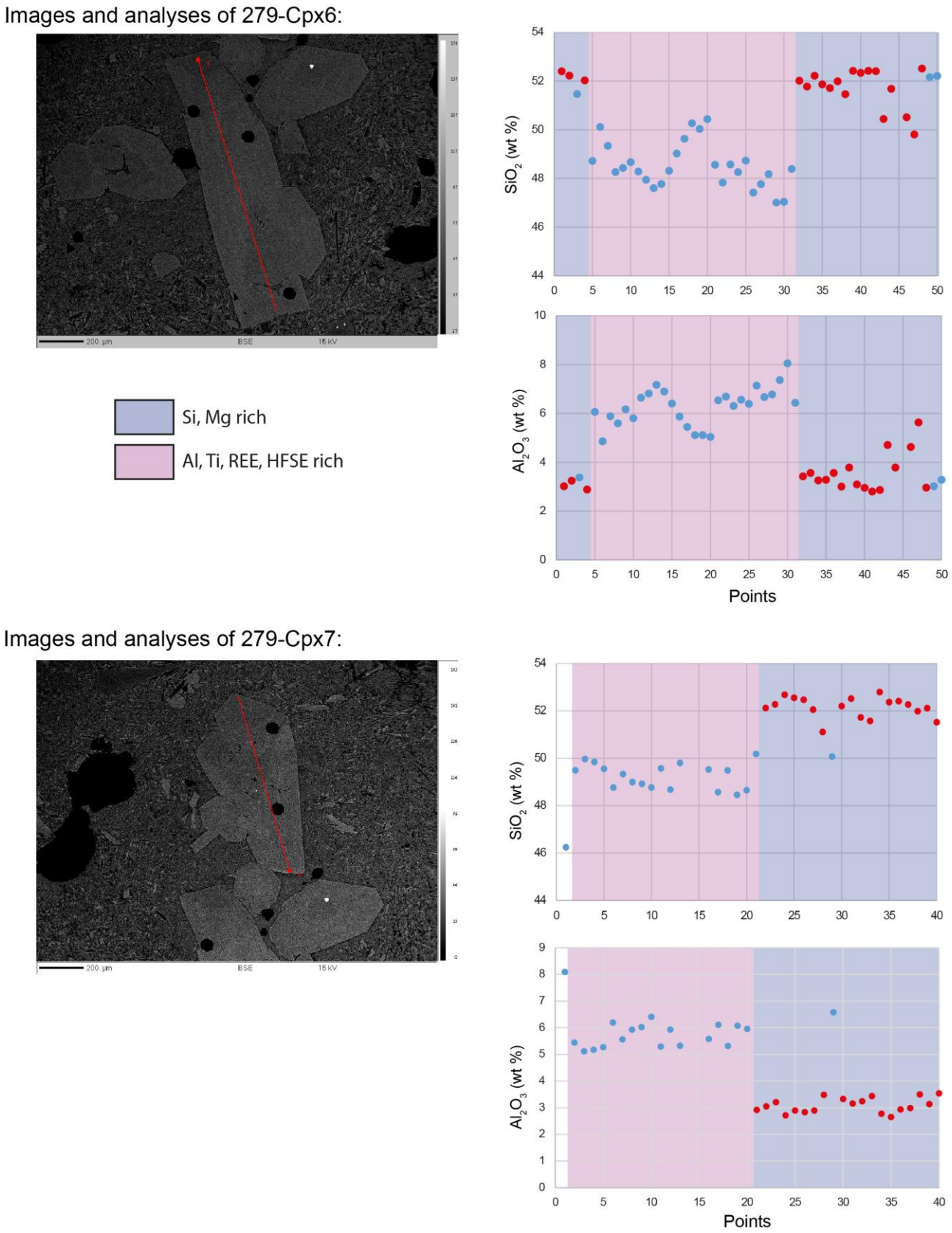

Figure S-16 BSE images and analysis profiles of Cpx6 and Cpx7 from SMA1974-279 used for geothermobarometric calculations. The red dots on the profiles are the points used for the geothermobarometric calculations (see Table S-20).

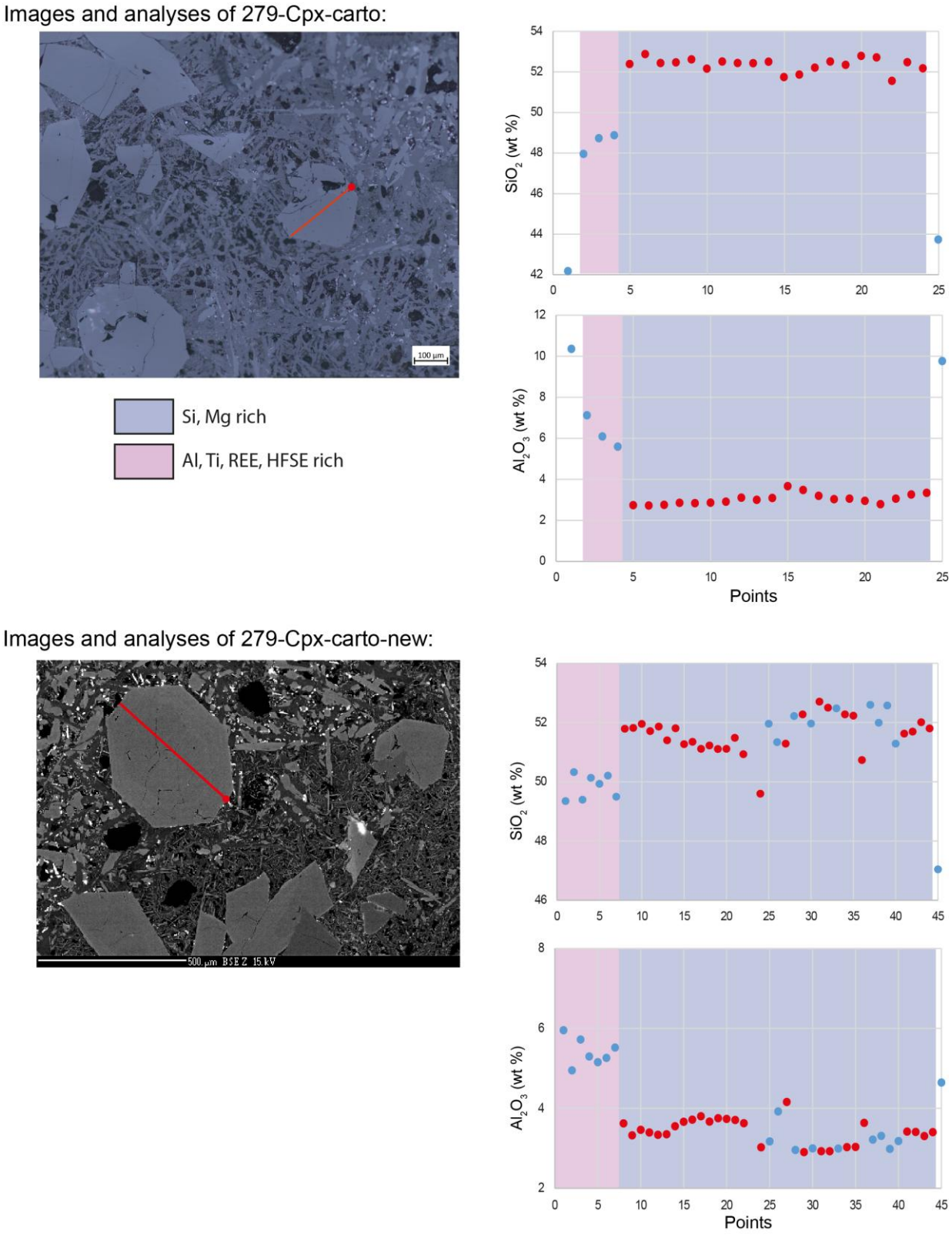

Figure S-17 BSE images and analysis profiles of Cpx-carto and Cpx-carto-new from SMA1974-279 used for geothermobarometric calculations. The red dots on the profiles are the points used for the geothermobarometric calculations (see Table S-20).

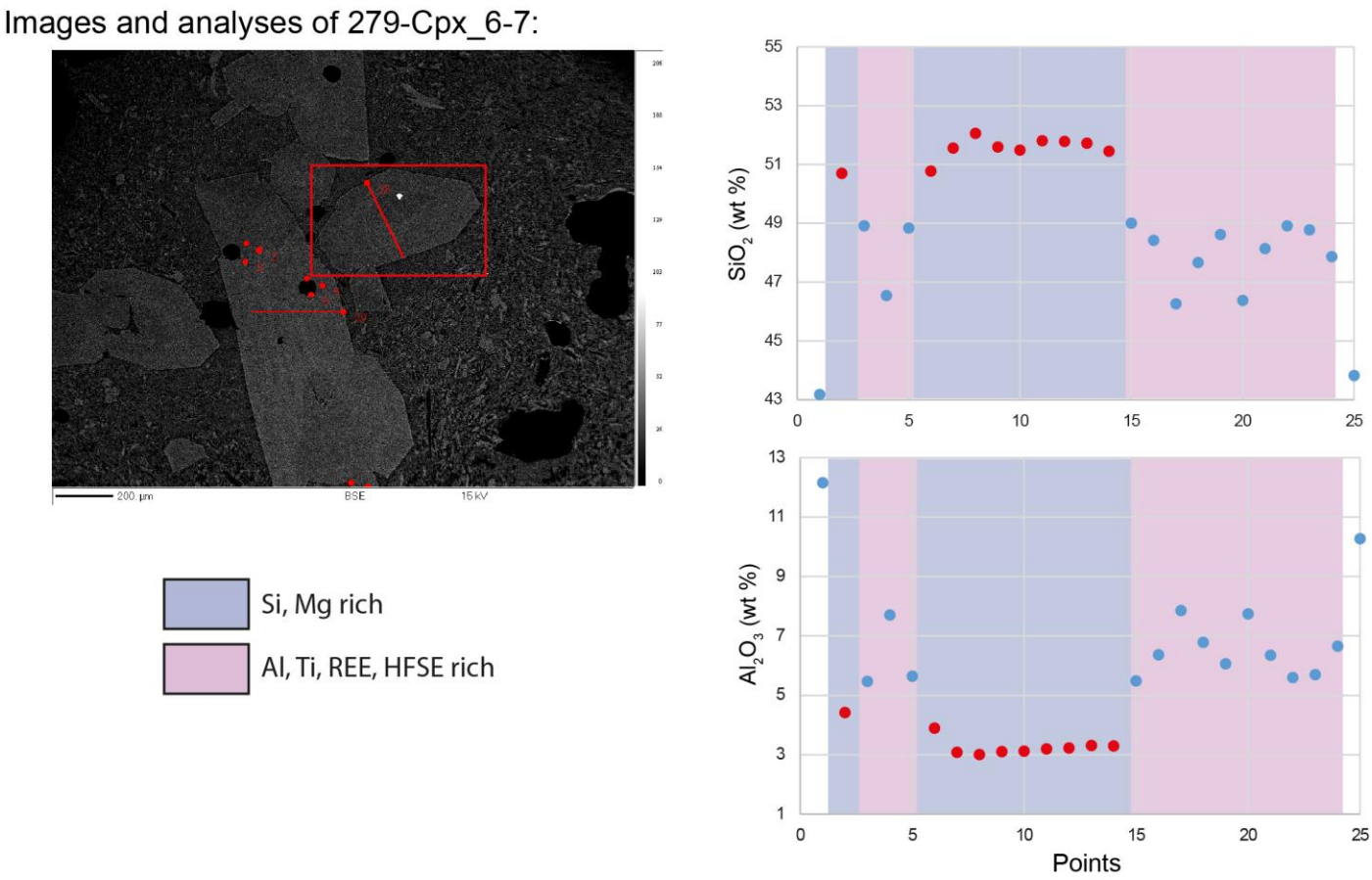

Figure S-18 BSE images and analysis profiles of Cpx6-7 from SMA1974-279 used for geothermobarometric calculations. The red dots on the profiles are the points used for the geothermobarometric calculations (see Table S-20).

Supplementary Information References

Barrat, J.A., Keller, F., Amossé, J., Taylor, R.N., Nesbitt, R.W., Hirata, T. (1996) DETERMINATION OF RARE EARTH ELEMENTS IN SIXTEEN SILICATE REFERENCE SAMPLES BY ICP-MS AFTER TM ADDITION AND ION EXCHANGE SEPARATION. *Geostandards Newsletter* 20, 133–139. https://doi.org/10.1111/j.1751-908X.1996.tb00177.x

Borghini, G., Fumagalli, P., Rampone, E. (2017) Partial melting of secondary pyroxenite at 1 and 1.5 GPa, and its role in upwelling heterogeneous mantle. *Contributions to Mineralogy and Petrology* 172, 70. https://doi.org/10.1007/s00410-017-1387-4

Brunelli, D., Verhoest, L., Ligi, M., Hemond, C., Maia, M., Soltanmohammadi, A., Lugli, F., Nonnotte, P., Cipriani, A. (2025) Large melt diversity at a mid-ocean ridge thermal low. *Science Advances* 11. https://doi.org/10.1126/sciadv.adv4654

Condamine, P., Couzinié, S., Fabbrizio, A., Devidal, J.-L., Médard, E. (2022) Trace element partitioning during incipient melting of phlogopite-peridotite in the spinel and garnet stability fields. *Geochimica et Cosmochimica Acta* 327, 53–78. https://doi.org/10.1016/j.gca.2022.04.011

Condamine, P., Médard, E. (2014) Experimental melting of phlogopite-bearing mantle at 1 GPa: Implications for potassic magmatism. *Earth and Planetary Science Letters* 397, 80–92. https://doi.org/10.1016/j.epsl.2014.04.027

Condamine, P., Médard, E., Devidal, J.-L. (2016) Experimental melting of phlogopite-peridotite in the garnet stability field. *Contributions to Mineralogy and Petrology* 171, 95. https://doi.org/10.1007/s00410-016-1306-0

Cotten, J., Le Dez, A., Bau, M., Caroff, M., Maury, R.C., Dulski, P., Fourcade, S., Bohn, M., Brousse, R. (1995) Origin of anomalous rare-earth element and yttrium enrichments in subaerially exposed basalts: Evidence from French Polynesia. *Chemical Geology* 119, 115–138. https://doi.org/10.1016/0009-2541(94)00102-E

Danyushevsky, L.V., Plechov, P. (2011) Petrolog3: Integrated software for modeling crystallization processes: PETROLOG3. *Geochemistry, Geophysics, Geosystems* 12, n/a–n/a. https://doi.org/10.1029/2011GC003516

Duvernay, T., Jiang, S., W. Ball, P., Davies, D.R. (2024) Coupled Geodynamical-Geochemical Perspectives on the Generation and Composition of Mid-Ocean Ridge Basalts. *Geochemistry, Geophysics, Geosystems*. https://doi.org/10.22541/essoar.169711689.99250544/v1

Grégoire, M., Bell, D., Le Roex, A. (2002) Trace element geochemistry of phlogopite-rich mafic mantle xenoliths: their classification and their relationship to phlogopite-bearing peridotites and kimberlites revisited. *Contributions to Mineralogy and Petrology* 142, 603–625. https://doi.org/10.1007/s00410-001-0315-8

Hellebrand, E. (2002) Garnet-field Melting and Late-stage Refertilization in "Residual" Abyssal Peridotites from the Central Indian Ridge. *Journal of Petrology* 43, 2305–2338. https://doi.org/10.1093/petrology/43.12.2305

Kendrick, M.A., Hemond, C., Kamenetsky, V.S., Danyushevsky, L., Devey, C., Rodemann, T., Perfit, M.R. (2017) Seawater cycled throughout Earth's mantle in partially serpentinised lithosphere. *Nature Geoscience* 10. https://doi.org/10.1038/ngeo2902

Kinzler, R.J. (1997) Melting of mantle peridotite at pressures approaching the spinel to garnet transition: Application to mid-ocean ridge basalt petrogenesis. *Journal of Geophysical Research: Solid Earth* 102, 853–874. https://doi.org/10.1029/96JB00988

Lambart, S. (2017) No direct contribution of recycled crust in Icelandic basalts. *Geochemical Perspectives Letters* 4, 7–12. https://doi.org/10.7185/geochemlet.1728

Marschall, H.R., Wanless, V.D., Shimizu, N., Pogge Von Strandmann, P.A.E., Elliott, T., Monteleone, B.D. (2017) The boron and lithium isotopic composition of mid-ocean ridge basalts and the mantle. *Geochimica et Cosmochimica Acta* 207, 102–138. https://doi.org/10.1016/j.gca.2017.03.028

Mollo, S., Putirka, K., Misiti, V., Soligo, M., Scarlato, P. (2013) A new test for equilibrium based on clinopyroxene–melt pairs: Clues on the solidification temperatures of Etnean alkaline melts at post-eruptive conditions. *Chemical Geology* 352, 92–100. https://doi.org/10.1016/j.chemgeo.2013.05.026

Neave, D.A., Putirka, K.D. (2017) A new clinopyroxene-liquid barometer, and implications for magma storage pressures under Icelandic rift zones. *American Mineralogist* 102, 777–794. https://doi.org/10.2138/am-2017-5968

Pertermann, M., Hirschmann, M.M., Hametner, K., Günther, D., Schmidt, M.W. (2004) Experimental determination of trace element partitioning between garnet and silica-rich liquid during anhydrous partial melting of MORB-like eclogite. *Geochemistry, Geophysics, Geosystems* 5, 2003GC000638. https://doi.org/10.1029/2003GC000638

Putirka, K. (1999) Clinopyroxene + liquid equilibria to 100 kbar and 2450 K. *Contributions to Mineralogy and Petrology* 135, 151–163. https://doi.org/10.1007/s004100050503

Putirka, K.D. (2008) Thermometers and Barometers for Volcanic Systems. *Reviews in Mineralogy and Geochemistry* 69, 61–120. https://doi.org/10.2138/rmg.2008.69.3

Sun, S. -s., McDonough, W.F. (1989) Chemical and isotopic systematics of oceanic basalts: implications for mantle composition and processes. *Geological Society, London, Special Publications* 42, 313–345. https://doi.org/10.1144/GSL.SP.1989.042.01.19

Van Der Zwan, F.M., Devey, C.W., Hansteen, T.H., Almeev, R.R., Augustin, N., Frische, M., Haase, K.M., Basaham, A., Snow, J.E. (2017) Lower crustal hydrothermal circulation at slow-spreading ridges: evidence from chlorine in Arctic and South Atlantic basalt glasses and melt inclusions. *Contributions to Mineralogy and Petrology* 172, 97. https://doi.org/10.1007/s00410-017-1418-1

Wang, W., Kelley, K.A., Li, Z., Chu, F., Dong, Y., Chen, L., Dong, Y., Li, J. (2021) Volatile Element Evidence of Local MORB Mantle Heterogeneity Beneath the Southwest Indian Ridge, 48°–51°E. *Geochemistry, Geophysics, Geosystems* 22, e2021GC009647. https://doi.org/10.1029/2021GC009647

Wieser, P.E., Kent, A.J.R., Till, C.B. (2023) Barometers Behaving Badly II: a Critical Evaluation of Cpx-Only and Cpx-Liq Thermobarometry in Variably-Hydrous Arc Magmas. *Journal of Petrology* 64, egad050. https://doi.org/10.1093/petrology/egad050

Workman, R.K., Hart, S.R. (2005) Major and trace element composition of the depleted MORB mantle (DMM). *Earth and Planetary Science Letters* 231, 53–72. https://doi.org/10.1016/j.epsl.2004.12.005

Yu, Z., Singh, S.C., Hamelin, C., Grenet, L., Maia, M., Briais, A., Petracchini, L., Brunelli, D. (2025) Deep mantle earthquakes linked to CO2 degassing at the mid-Atlantic ridge. *Nature Communications* 16, 563. https://doi.org/10.1038/s41467-024-55792-9

Zhou, J.-S., Wang, Q., Xing, C.-M., Ma, L., Hao, L.-L., Li, Q.-W., Wang, Z.-L., Huang, T.-Y. (2021) Crystal growth of clinopyroxene in mafic alkaline magmas. *Earth and Planetary Science Letters* 568, 117005. https://doi.org/10.1016/j.epsl.2021.117005